

Research Strategy

Significance

Integrating magnetic resonance imaging (MRI) functionality with radiation therapy (RT) linear accelerator (LINAC) can better render the visualization of the soft tissues of lesions and surrounding healthy organs-at-risks (OARs) during cancer RT treatment planning and procedures. This is because MR scans, in contrast to the prevalent computed tomography (CT) scans used in clinics today, provide a richly contrasted image of internal body tissues. More importantly, MRI-LINAC integration can be done in an unrivaled, online, and real-time fashion to aid a more precise radiation dose delivery in RT [1]. There are now MRI-LINAC systems such as Raaymakers et al's [1,5], which was later commercialized by Elekta AB (Sweden) [1]. The MRIidian system is another one of such technologies, essentially an MRI-based image-guided RT [6], developed by Viewray (USA). There is also the Aurora RT system from MagnetTx (Canada) [7], or the non-commissioned Australian MRI-Linac project [8]. While MRI-LINAC integration has been widely researched [1,5,9,10], the effect of random and involuntary patient motion causes motion artifacts which lowers the quality of MR imaging scans for use in brain and head and neck (H&N) RT. These artifacts in image collection lower the accuracy of online and real-time precise radiation dose delivery, which in turn affects clinical efficacy.

During RT, it is paramount to keep the patient accurately positioned on the treatment table, especially in applications aimed at more precise irradiation such as in head and neck cancers. The importance of accurate patient positioning is further underscored by accumulating evidence that patient displacement and collimator and gantry angle misalignment during RT showed high sensitivity to small perturbations: a 3-mm error in anterior-posterior direction caused 38% decrease in minimum target dose [11]. Thus, to automatically align patient motion during RT, state-of-the-art clinical approaches use either a frame or a mask to stabilize patient motion on the treatment couch.

Known roles of frames in positioning compensation

In frame-based approaches, a metal ring (the Brown-Robert-Wells frame) is attached to the patient's skull using screws, and then bolted to the treatment table, Fig. 1a. Discomfort and severe pain often results from long hours of minimally invasive surgery where the skull is fixed with pins for head immobilization during stereo-tactic radiosurgery (SRS). The invasiveness and discomfort associated with the frame are a principal cause of poor patient compliance and poor clinical efficacy. For some patients, frame placement is not feasible due to extreme cranial anatomy or prior surgical bone flaps. In cases where multiple radiation therapy (RT) deliveries are needed, patients cannot be subjected to daily attachment and removal of the frame.

Known roles of masks in positioning compensation

These limitations of frames have spurred clinics to start using thermoplastic face masks. Here, a porous mask is deformed to fit the geometry of the patient's head and neck region and then fastened to the treatment table. As the mask is flexible, during the course of treatment, it loses its firmness around the patient so that the inaccuracy of dose targeting is inevitable. The flexibility of masks has been identified to cause a drift of up to 6mm. This is unacceptable given the AAPM TG-42 positioning accuracy guidelines that specify < 2 mm accuracy [14]. Changes in the mask's physical texture from repeated application and shrinking, Fig. 1b, can also lower treatment accuracy. These inconsistencies are not suitable for deep tumors located nearby critical structures such as the brain stem or for newer treatment modalities such as single isocenter multiple-target SRS, which are highly sensitive to rotational head motions. Even so, conventional LINACs used at most cancer centers are insufficient for the high geometric accuracy and precision required of SRS for isocenter localization [15].

Known roles of rigid robots in positioning compensation

To overcome these issues, explorative robotic positioning research studies have demonstrated the feasibility of maintaining stable patient cranial motion consistent with treatment plans. For example, the Wiersma Lab's Stewart-Gough (SG) platform [2, 16, 17], illustrated in Fig. 1(c), achieves $\leq 0.5\text{mm}$ and $\leq 0.5^\circ$ positioning accuracy 90% of the time. It is constructed as a 6-6 SG platform out of linear

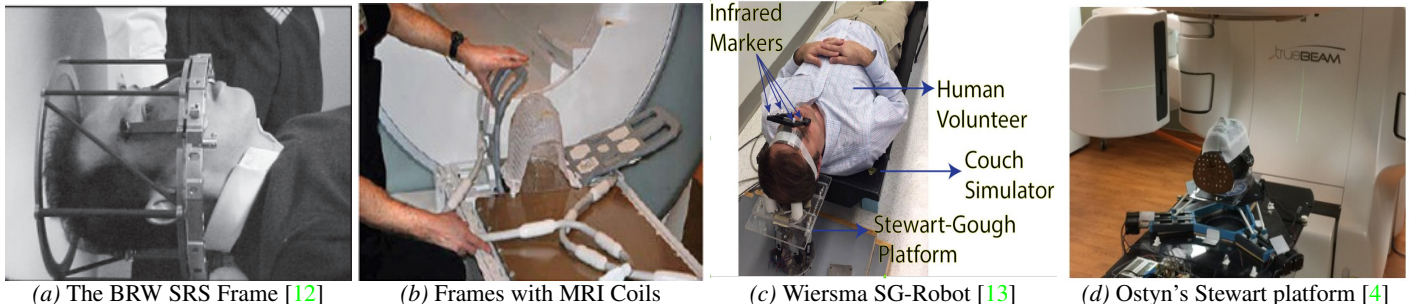


Figure 1: Existing frame and mask (a-b), and frameless and maskless robotic systems (c-d).

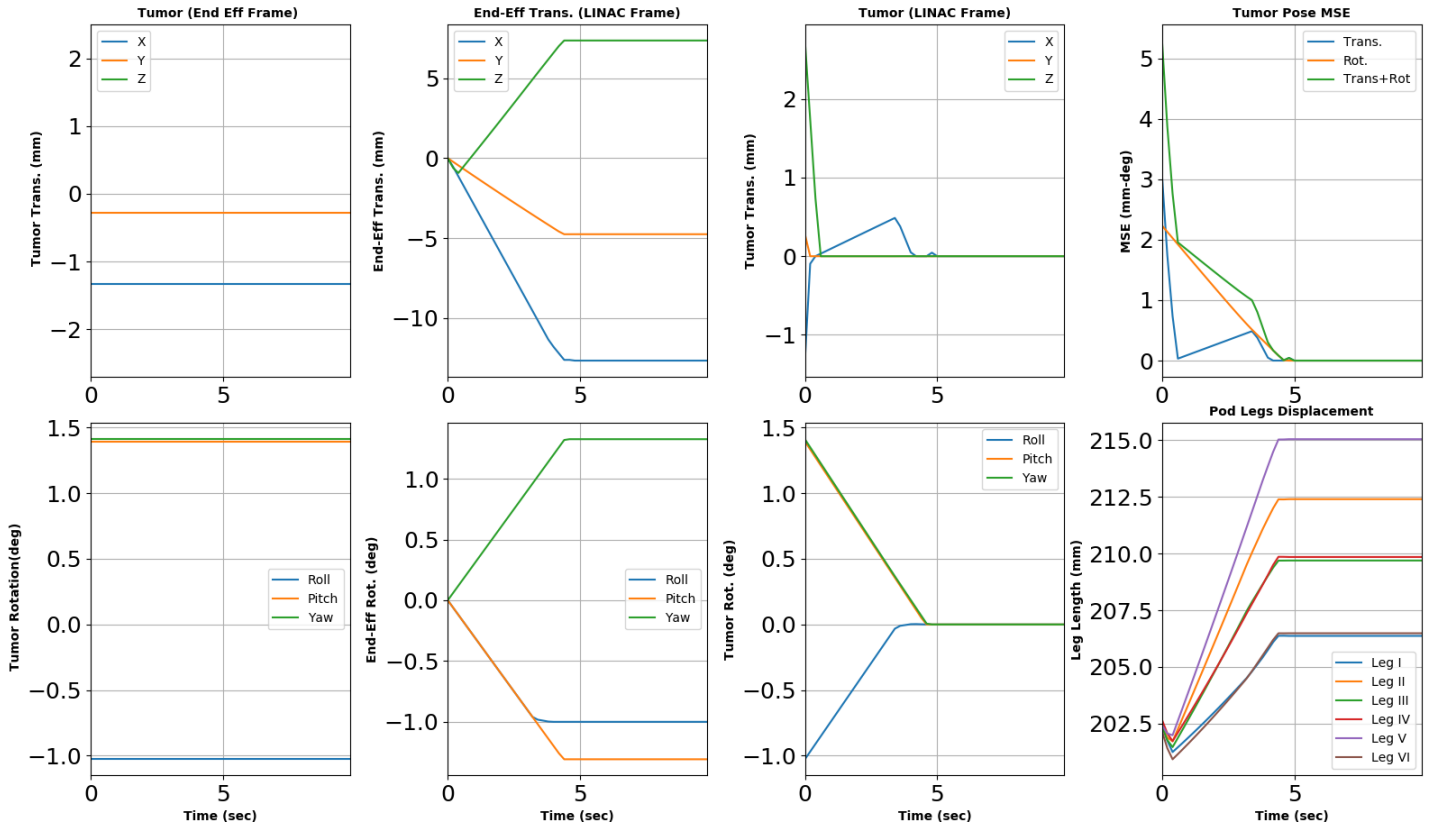


Figure 2: Isocenter Head Stabilization Results Using the Wiersma Rigid Stewart-Gough Platform. Reprinted with permission from [17].

actuators, electric motors and rigid metallic components. While effective at head position compensation in SRS treatment procedures, it is not adaptable for new MRI-integration with LINAC RTs that offer better real-time soft tissues delineation for a precise irradiation. The Ostyn et al research group sought to alleviate this rigid structure by 3D printing the mechanical components of the Stewart-Gough platform [4]. It is worth noting, however, that this platform uses stepper motors as well (see Fig. 1(d)) to actuate the legs of the robot. This by nature leads to radiation attenuation. With the potential to aid better clinical accuracy in SRS-based systems when commissioned, these systems are not suitable for the emerging MRI-LINAC machines. This is because they utilize rigid metallic components, electric motors and linear actuators which are not suitable for the large tubular magnets of the MR machine: they interfere with the magnetic fields of the MR machine and have been known to lead to patient fatality or significantly damage the MR machine when clinicians have been careless about bringing metallic materials into the treatment room [18].

Published work from the Wiersma lab shows that a rigid parallel robot can provide the online, real-time patient motion compensation in mock SRS and RT treatments (see Fig. 2). Here, using an L-BFGS-based trajectory optimization formulation for patient head motion compensation, the algorithm was able to maintain a $\leq 0.5\text{mm}$ and $\leq 0.5^\circ$ clinical tolerance objective for 100% of the treatment time [17]. But observe that not all constraints are adhered to: for example, observe the overshoot along Z for the tumor in the LINAC frame and the wriggly trajectories along the rotational axis of the tumor before it reaches steady state. Furthermore, while this robot does work well for SRS treatment procedures, it does not translate to integrating MRI functionality with LINACs owing to its structural mechanical characteristics.

Known roles of soft robots in RT

My preliminary work on soft manipulators for patient head motion compensation in RT shows that novel soft robot manipulators can compensate head motion within the submillimeter and subdegree accuracy of the AAPM-TG42 stipulation for up to 3 DoFs [19–22]. In a cascaded PID-PI controller loop, I initially showed head motion correction for head setpoint- and trajectory-following to be accurate to within $\leq 1.5\text{mm}$ for a task of lowering or raising the head along on a treatment table [19]. These results are duplicated in Fig. 3. Furthermore, Fig. 4 illustrates the testbed I used in generating the 3-DoF control results of Fig. 5. Here, the setup consists of a phantom with a neck simulator that models the ball joint in the human torso. A vision-based 3D sensor acquires the face's point cloud in real-time, which is then processed for features-extraction and the 6D coordinates of the head (here using the tip of the nose) are sent to a microcontroller (National Instruments®myRIO); the myRIO then regulates the flow of compressed air into a set of proportional solenoid valves. The amount of air within the set of inflatable air bladders (IABs), in turn raise, lower, or tilt the head on the mock treatment table. The dynamics of the head interaction with the IABs and air pressure supply were carried with a lumped prediction error model [23].

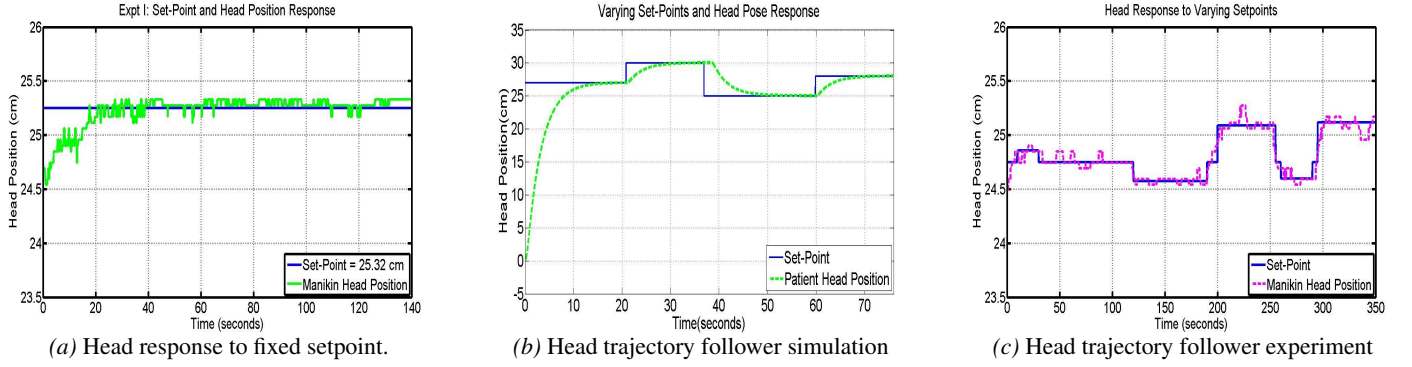


Figure 3: 1-DoF Online, Real-Time Head Motion Correction. Reprinted from [19].

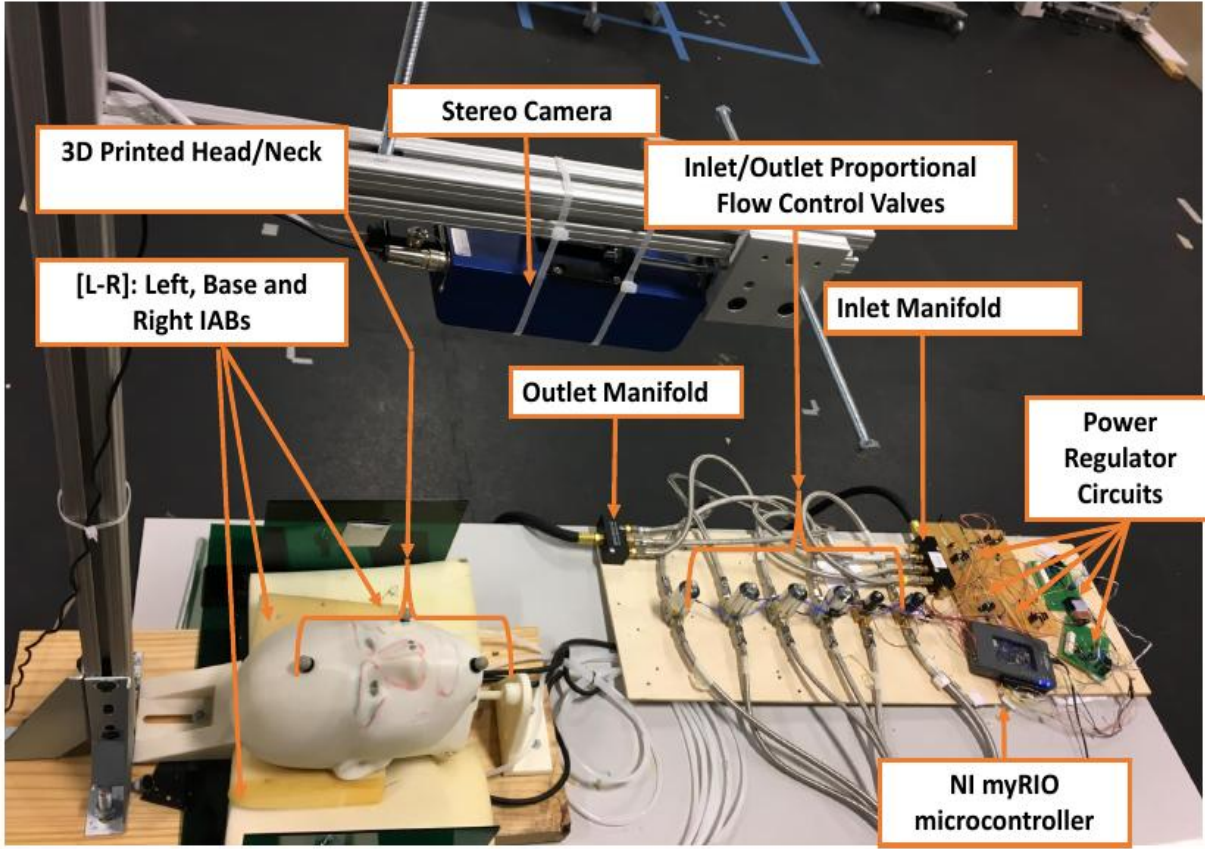
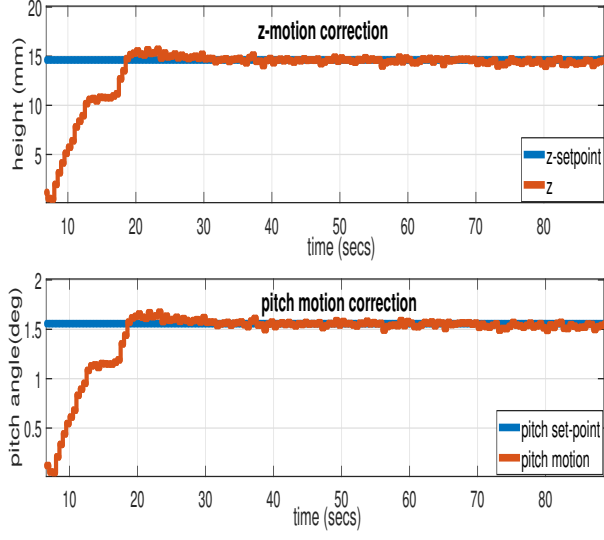


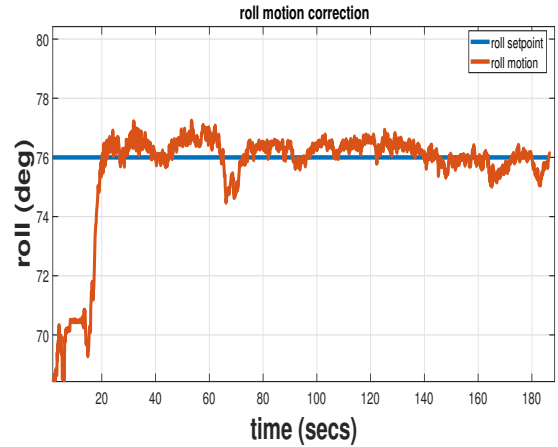
Figure 4: Three DoF Testbed. Reprinted from [20].

This model was then used in a controller that leveraged indirect model reference adaptive control with optimal state regulation in order to ensure the head follows set trajectory through steady-state [20]. Some of these results are reprinted in Fig. 3 and Fig. 5 respectively.

Now, in a new class of soft actuator designs, and contrary to stochastic system identification techniques I used in my previous models [19,20,22], we can now specifically regulate volume fractions within the IABs as well as accurately control their spatial deformations based on specific nonlinear elastic deformation relationships [24]. Being continuum, compliant and configurable (C3) for manipulation tasks, we recently demonstrated in control experiments that they are well capable of providing patient head motion compensation [13]. Contrary to remote-controlled airbags that have been used in upper mandible and head manipulation [25], our actuators deform based on their material moduli, compressed air pressurization and incompressibility constraints when given a reference trajectory. To our knowledge, ours are the first to explore C3 materials as actuation systems for cranial manipulation in robotic radiotherapy. Deforming based on prescribed internal pressurization, their surface displacement errors are accurate to the order of $< 1.5 \times 10^{-4} \text{ mm}$ [24]. These results are reiterated in Fig. 6 where a spherically-textured soft actuator was prescribed to deform from an initial internal radius, $R_i = 2.7 \text{ mm}$ from

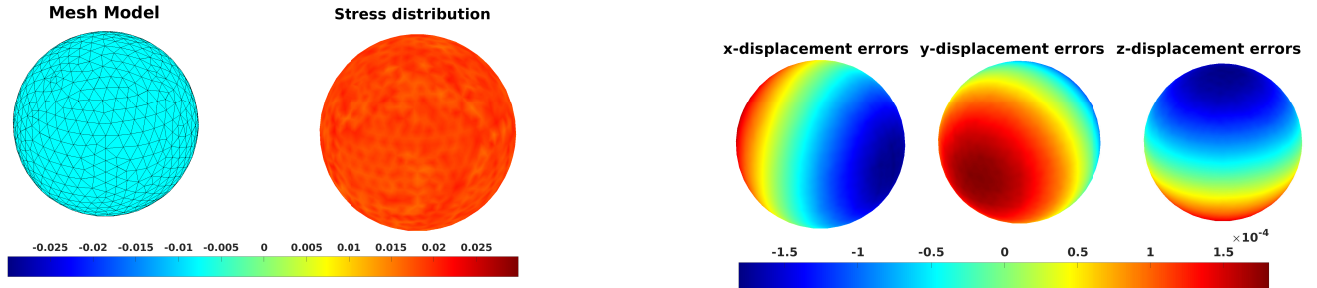


(a) Z and pitch motion correction.



(b) Roll motion correction.

Figure 5: 3-DoF Online, Real-Time Head Motion Correction. Reprinted from [20].



(a) Left: Mesh model. Right: Stress distribution post-defomation.

(b) Displacement errors along x, y, z coordinates.

Inputs					Outputs		
C_1	C_2	$R_i(\text{mm})$	$r_i(\text{mm})$	$R_o(\text{mm})$	$r_o(\text{mm})$	$P(\text{psi})$	ΔV
$1.1e4$	$2.2e4$	2.7	3	3	3.3	.76	≈ 0

Figure 6: Volumetric Deformation of a Soft Actuator (Expansion). Reprinted from [24].

the reference configuration to $r_i = 3.3\text{mm}$ in the current configuration. Based on my derived constitutive relation between the applied pressure and the radius of the actuator, a pressure of 0.76 psi was found to be suitable to realize this deformation. The charts of Fig. 6 illustrates the response of the actuator based on a prescribed pressure, where C_1 and C_2 are appropriate material moduli. With the standard local volume preservation principle, we notice a displacement error of 1.5×10^{-4} along the rectangular Cartesian coordinates and a zero volumetric change i.e. $\Delta V \approx 0$. This shows that with *highly accurate pressure sensors*, and equipped with properly calibrated proportional solenoid valves, we can regulate the air within a soft actuator's chamber so that specific and highly precise deformation behaviors are realizable for consumer soft actuators.

Hypothesis

My **leading hypothesis** is to use MRI/LINAC-compatible soft robot system that can provide 6-DoF head motion correction in precision RT procedures to serve as a viable alternative to current mask-based as well as frameless and maskless robot-based cranial manipulation systems. In this sentiment, **I hypothesize that time-resolved MRI-LINAC techniques, which provide superior soft tissue scans, in conjunction with non-magnetic and radiation transparent soft robots can provide superior brain or H&N radiation dose targets for precise MRI-LINAC RT treatment procedures.** Existing frame-based immobilization devices, Fig. 1a, and frameless and maskless rigid robotic motion correction mechanisms, Fig. 1c&d, are not suitable for this because of their electro-mechanical parts that introduce serious safety concerns. Furthermore, **I hypothesize that an asymptotically stable in the large and optimal motion-planner can find collision-free paths**

that satisfy head motion constraints can resolve the abnormalities inherent in current controllers used in head motion correction systems [2, 3, 16, 20]. This will alleviate the overshoots experienced during head motion correction as illustrated in Fig. 2. I will test this leading hypothesis to see if 6-DOF target motion of a patient is ≤ 0.5 mm and $\leq 0.5^\circ$ for greater than 95% of the treatment time using MRI imaging for soft robot-based motion compensation.

Along with other experiments where I verified that vision-based control of soft robots can geometrically correct patient motion precisely fast-enough in real-time up to three DOFs [19–22], and existing hybrid MRI-compatible RT systems [5, 9, 10], we will test these hypotheses that soft robots can provide position accuracy that is consistent for use in standalone MRIs, MRI-LINAC RT systems or SRS-alone treatment procedures in order to (i) negate the deleterious effects of *interfractional* setup variation on patients; (ii) correct the complex *intrafractional geometric uncertainties* such as posture changes, and body deformation with minimal invasiveness; (iii) eliminate radiation attenuation associated with the metallic components of frames and rigid robotic patient motion compensation systems; and (iv) correct the flex associated with thermoplastic face masks; while *not interfering with the MR machine's magnetic field*.

Innovation.

Conceptual Innovation

My work was the first to demonstrate the feasibility of vision-based 3 DOF control of soft manipulators for cranial motion management in RT [19–22]; we are extending this to 6-DOF control with my novel advanced mechanism

- The newly proposed mechanism is made entirely of no metal (hence not susceptible to magnetic fields) and is radiation-transparent so that it is compatible with both MRI-LINACs.
- This mechanism can be adapted to confined spaces under MRI coils (see Fig. 1b) given its compactness, and light weight.
- It possesses little invasiveness to the patient.
- It Exhibits a quick-connect, quick-disconnect modularity on a couch – important for patients with varying cranial anatomy – thus easing the logistical setup workload of current immobilization and maskless robotic systems.

Technical/Healthcare Innovation

To our knowledge, **no currently-available technology exists today that can perform real-time head position stabilization without dose attenuation in an online, real-time fashion whilst guaranteeing patient safety similar to our proposed MRI-LINAC non-magnetic and radio-transparent soft robot RT positioning system**. As photon-based cancer treatment accounts for > 50% of all cancer treatments [26], these exploratory experiments are relevant to public health and have transformational clinical potential because they may provide (i) proof-of-concept evidence that soft robots are compatible with standalone MRI imaging modalities; (ii) evidence of precise and automatic motion management with non-magnetic and radiation-transparent soft robots in emerging hybrid MRI-accelerator RT; (iii) an emergence of a better brain and H&N cancer management technology that can be adapted to confined spaces under MRI coils (see Fig. 1b). Upon successful completion, this soft robot will be used for active head motion stabilization within an MR machine. It will be adaptable for standalone MRIs, emerging MRI-LINAC technologies, and brain as well as H&N RTs. It will provide accurate RT beam targeting as well as preventing patient motion MRI imaging artifacts. This technology will improve therapeutic outcomes, and eliminate patient invasiveness.

Approach.

K₉₉ Aim I: To Develop a Distributively-Innervated, Non-magnetic, and Radiation-Transparent Soft Actuator.

Rationale: For though the design of Fig. 4 is relevant to head motion control on an RT treatment table, it is not a complete motion correction system owing to its underactuated mechanism: it is only able to correct motion for up to three DoFs. Motion of the head occurs along six DoFs and they are not independent. Therefore, to realize a full patient motion compensation, more actuators are needed in the mechanism. To this end, and iterating further on my previous designs [20–22], I now propose a new class of continuum, compliant and configurable (C3) light, and agile soft actuators [24, 27, 28] which are the composition of a non-magnetic and radiation-transparent soft robot for use in MRI-LINACs to further aid dose delivery precision. The component soft actuators are planar and circular in their reference configuration. Upon compressed air actuation, they deform along the radial direction (see computer model in Fig. 7) based on the physical constraints baked into the elastomer-fabric matrix. This actuation design is inspired by the behavior of the skin papillae of certain Cephalopods (octopus, cuttlefish, bivalves and mollusks) which can transform their physical texture from 2D to 3D in less than 2 seconds [29, 30]. The actuators exhibit a radially symmetric deformation and are constrained along their circumferential axis under pneumatic actuation based on their novel design. There exists no electrical wirings or embedded electronics to assure that the actuators reach a desired configuration.

Hypothesis: Based on previous success of air actuated elastomeric chambers for manipulating patient head motion correction in real-time, I hypothesize that a fully-compliant and parallel soft robot can effectively correct patient head motion (given a robustly stable and

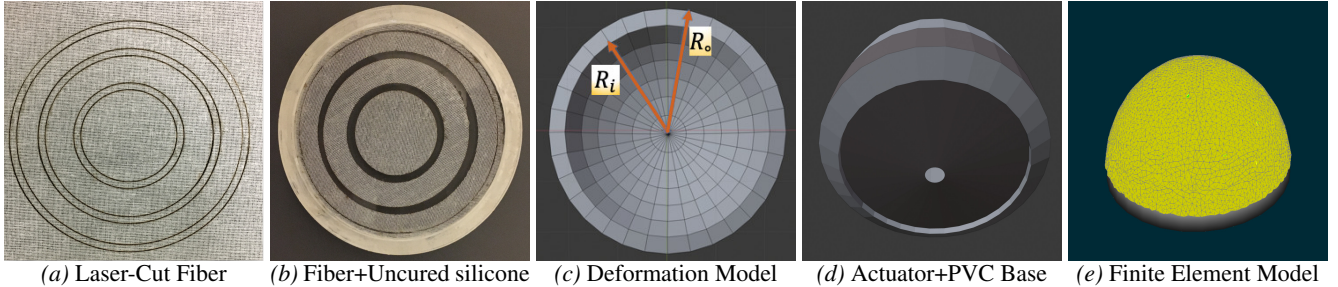


Figure 7: Soft actuator fabrication procedure.

optimal controller) such that the motion artifacts that are prone in MR imaging can be eliminated. This will assure an improved RT treatment outcomes in modern MRI-LINAC RTs.

Procedure.

A. Soft Actuator Design: The soft actuator fabrication methodology is illustrated in Fig. 7. A thin-layered fabric is laser cut into circular patterns (Fig. 7a), the cut meshes are removed and laid onto uncured silicone (Fig. 7b) which has been poured into a mold. We further add a silicone topcoat layer to the fabric before we allow it to cure at room temperature. Upon low pneumatic pressurization, the cured rubber deforms, obeying a Circumferentially-COnstrained And Radially Stretched fiber-Elastomer (CCOARSE) property [31] (Fig. 7c). This unique deformation pattern is similar to the way a balloon would stretch along its axial direction if a rope were tied around its circumference. The soft robot, after cure, is laid onto an impact-resistant, low-temperature rigid PVC insulation foam sheet, encased in a carbon fiber material. This aids radiation transparency (Fig. 7d). The finite elastic deformation mesh model of the soft robot for simulation purposes is shown in (Fig. 7e). This proposed fabrication method allows us to rapidly iterate different designs using compressed low air pressure (1-15 psi) that is (i) cheaply available, (ii) environmentally-friendly, (iii) avoids electrical wirings, (iv) is lightweight, and (v) inviscid which will make the soft robot adaptable for MRI-LINAC systems – creating a clean and safe human-robot workspace. As the air inflow into the chambers of the elastomers need to be carefully regulated, we will build current source electronic regulator circuits that proportionally vary the amount of airflow though connecting hoses that lead into the proportional solenoid valves used in earlier experiments [20].

B. Pneumatic System Design: We now describe the integration of the soft actuator design proposed above with the rest of the pneumatic actuation system. This system is illustrated in Fig. 8. A self-contained compressed air canister supplies air at a fixed pressure (e.g. 15 psi) through a firm polyurethane air tubing into a 4-20mA output-M12 pressure transducer plug connection. The choice of pressure transmitter is important owing to the accuracy requirement for air volume within the chamber of the soft actuator. In our experience, the G2 series of pressure transducers from Ashcroft® are an excellent choice for such application as this: it offers a $\pm 1.00\%$ total error band accuracy; being highly configurable, it offers a pressure range that meets our actuation needs and it can be easily integrated into our overall mechanism. The outlet of this pressure transmitter conveys the airflow into a proportional solenoid valve. We use proportioning valves to control the amount of airflow into the actuator’s air chamber because of the air flow precision requirement needed to correctly manipulate the head. The outlet of this solenoid valve then leads to the inlet air connector of the soft actuator. The electronic regulating circuit shown in Fig. 8 is a standard current source circuit that varies the air flow rate within the proportional valve by adjusting the current flowing through its shunt resistor. In addition, a venturi pump removes air at a proportional pressure compared to the inlet supply pressure. This pressure differential helps maintain head along a setpoint or follow a varying trajectory.

C. Preliminary Actuation Experiments: We have initial experiments that reproduces deformation behavior similar to the spike observed in the skin papillae of the Octopus. This is described in what follows. We cast silicone from Smooth-On Inc’s dragon skin (475 psi tensile strength and 10A shore hardness), whose material properties exhibit enough softness for patient comfort and enough firmness that withstands extremely nonlinear deformation from the wrench produced by the typical human head (55-65 kg [32–34]. The ingrained fabric membrane within the elastomer imposes the CCOARSE property, constraining the circumferential expansion of the rubber and exerting a radially symmetric stretch as shown in the bottom row of Fig. 9. This considerably simplifies the dynamics model that governs the deformation [28]. Two different designs are shown in the top and bottom rows of Fig. 9. The rubber material is screwed onto a bottom PVC foam sheet using a laser-cut acrylic planar ring. We use **nylon** Phillips screws. The behavior at different levels of pressurization are indicated in each column of the figure. The top row shows the cured silicone without fabric while the bottom row shows the silicone with the entrenched fiber matrix within the elastomer. As can be seen, the material in the top row exhibits a circumferential bulge as well as radial bulge while the ones in the bottom row only extend along the axial direction. As can be seen in the bottom row, we can generate a full *Gaussian deformation* and return to the reference planar configuration in 2 seconds (see more images and videos in scriptedonachip.com/soro) similar to the spikes produced by the skin papillae of the Octopus. These quick Gaussian spikes will be useful for rapid head motion correction in MRI-LINACs. The soft compliance and tensile strength of this silicone material make it well-suited for treatment procedures where non-magnetic and radiation-transparent components can boost stereotactic precision as well as improve tumor control in MRI-LINACs.

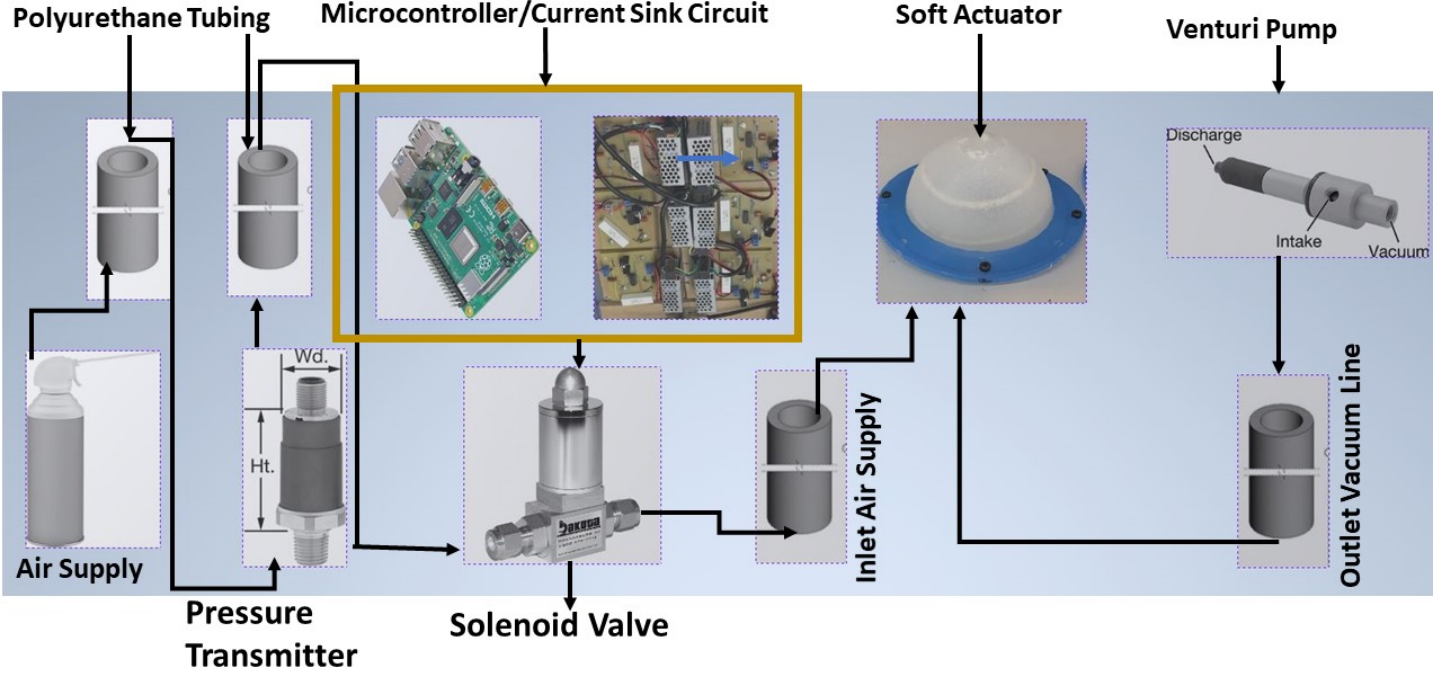


Figure 8: Pneumatic System showing proportional solenoid valve, electronic pressure regulators and raspberry pi microcontroller.

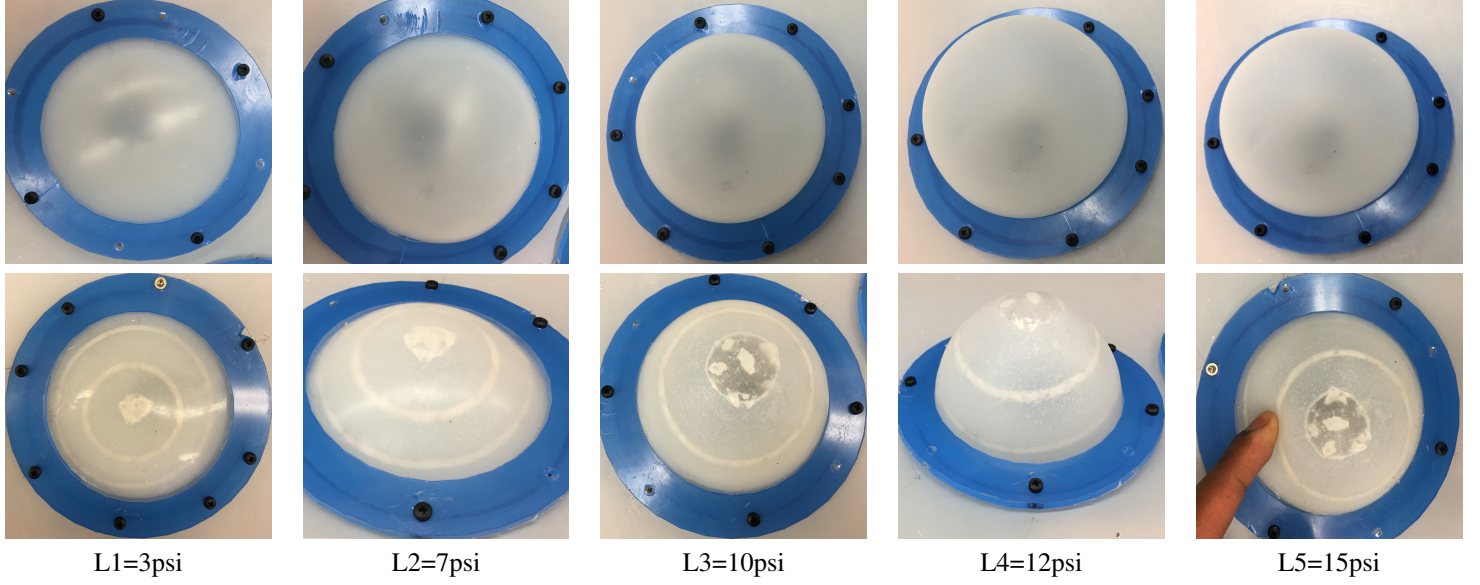


Figure 9: Deformation Levels of elastomer (top) and Elastomeric-Fiber Matrix (bottom) under Low Air Pressurization (3-15psi).

D. Flexible Piezoresistive Distributed Sensor Integration: In a recent formulation [24], we mapped the relationship between the applied pressure to the deformed radius of a soft actuator using the standard Mooney-Rivlin formulation [35, 36]. Suppose that C_1 and C_2 are appropriate material moduli for the soft actuator, then the applied pressure in the internal walls of the actuator is given by the relation

$$P(r) = \int_{r_i}^{r_o} \left[2C_1 \left(\frac{r}{R^2} - \frac{R^4}{r^5} \right) + 2C_2 \left(\frac{r^3}{R^4} - \frac{R^2}{r^3} \right) \right] dr \quad (1)$$

where r_i and r_o are respectively the internal and external radius of the actuator walls in the current configuration, and they have corresponding forms R_i and R_o in the reference configuration. Taking cues from the precise control schemes of rigid robot manipulators made possible by presence of joint encoders and harmonic drives that enable precise control of the joint angles between robot links, a means of sensing the “measure of deformation” based on the amount of pressure in the actuator’s air chamber is necessary for a successful control.

There have been various measures proposed in literature over the past few years about sensing volumetric deformation of a soft actuator. For example, embedded optically-laced fiber sensors based on the principle of frustrated total internal reflection, and distributed throughout a 3D printed elastomer, were used to generate a cointegrated body, sensing, and communication network for a soft robot’s state sensing [37]. They have also found applications in innervated soft finger prosthetic hand designs [38], where a very lossy optical waveguide was used in an open-loop control setting to detect shape and texture. While in softness grasp dexterity, they appear promising, they are not yet suitable for human-level texture-based sensitivity (nanometers) despite their complex design. Stretchable sensors with rheological properties have been erstwhile embedded within an elastomer using 3D printing techniques [39]; and though they have been shown to be mechanically receptive, and scalable up to e.g. $\sim 400\%$ strain, their electrical resistance gives at strains $> 400\%$ owing to the percolation of the networked components [39]. Pneumatic actuator networks patterned within an elastomeric robot body via a multi-material, embedded 3D printing technique have been tried [40]. Dielectric elastomers (DE) making use of the static charge properties of passive electronic components have been shown capable of measuring strain by up to 1692% under the Maxwell pressure law [41]. This DE actuators generally rely on electrostatic voltage discharge to sense deformation [42].

Owing to our precise manipulation requirement, a richly innervated means of sensing actuator deformation at high strains (owing to large reactive head forces) is necessary for effective closed-loop feedback control of head motion. Borrowing cues from the observational and short/long-term learning skills arising from the afferent neural networks on the exteroceptive skins of Cephalopods [30, Ch. 2], we will integrate volumetric tactile mechano-receptors on the soft actuators’ skins. As we aim to avoid rigid electro-mechanical sources that can hamper radiation delivery within the design, we will shun DEAs. Optical waveguides would be attractive but they are expensive to integrate for volumetric sensing. Instead, I propose tactile stretchable kirigami sensors made out of polyimides (Kapton sheets) and fiberglass membranes. Meso-scale stretchable Kirigami layer-by-layer manufacture of soft robots have recently been shown to be relevant for fast and precise deployment of robots [43, 44] with high sensing accuracy . Even so, the 3D perception of the environment of these piezoresistive innervated soft robot skins can be perceived using deep learning [45]. In this sentiment, I will laser-cut electrical grade Kapton sheets, weave them in twisting formations with fiberglass materials to mimic the bending of beams that enable accurate sensing [43]. The sensors will then be neatly covalently bonded (without adhesives) to the soft actuators surface by plasma treatment [46]. The proprioception of the soft actuators will be captured by an LSTM deep-learning network such as I used in my previous works [47–49]: this will predict the configuration of each soft actuator during both prescribed and random actuation sequences, even with feedback from non-monotonic, hysteretic, soft piezoresistive sensors. This fabrication approach is attractive because (i) it allows the separation of the fabrication of the soft actuator design from the piezo-resistive sensors; (ii) we can separately characterize the deformation sensing properties of the piezoresistive fiberglass-polyimide sensors for QA purposes before respective integration onto the component actuators; and (iii) it offers a modular and cheap fabrication design methodology that eases troubleshooting during the construction phase.

E. Expected results: I expect to see individual soft actuators obeying the prescribed pressure law given in (1) so that the deformation radius of the actuators exactly follows an applied pressure similar to the presented simulation results of Fig. 6, further elaborated in [24]. In addition, as I am skilled and well-versed in inference using deep-learning methods (see representative publications [47, 48, 50, 51]), I expect that the stretchable Kirigami sensor layers embedded within the elastomeric actuator membranes will produce rich innervated data that can be processed with deep learning based methods [45] for onward control processing.

K₉₉ Aim II: To Develop a Multi-Modal and Robustly Stable Optimal Motion-Planner.

Rationale: Current SRS-based immobilization and head motion compensation techniques are pre-programmed and heavily calibrated within their environment in order to find the optimal and safest path required in moving a patient’s cranial structure from one location to another in the robot workspace [3, 13, 16, 52, 53]. Techniques used range from PID control schemes [2, 19], reduced-order observer feedback control design [22], optimal and robustly stable indirect model reference adaptive control design [20], to local trajectory optimization schemes [17]. While these schemes work manually for specific automation task, they require extensive calibration and adjustment of parameters so as to get them to work in each new environment and for every new head motion control task. For these robots to execute tasks autonomously, a motion planning system capable of generating feasible motion from high-level requirements is needed. In addition, this motion planning system must respect the constraints on a task in order achieve success, such as turning the translating the head about its cranial-caudal axis, or rotating the head about its neck fulcrum. *I will reformulate these control tasks into a manifold-constrained geometric motion planning problem, concerned with finding a feasible optimal and collision-free path for a patient’s head motion.*

In order to optimally move the patient’s head in an optimally safe and collision-free path that avoids the exposure of normal tissues to high radiation dose, and is not task-dependent, it is important to develop a motion-planner that (i) executes head motion in the robot’s workspace by first finding a collision-free path; (ii) improves the plan into a better plan if the original plan is not efficient or does not satisfy C-space constraints; this may involve multiple iterations; (iii) considers how to move the head along a path that is stable and robust for execution in spite of modeling errors and uncertainties, while maintaining various speeds that satisfy various momentum

considerations; and lastly (iv) the found plan must be included in a hierarchical planning framework so that the original plan reaches termination, in order to allow larger plans in the hierarchy to roll out as needed. This planning approach is consistent with motion planning algorithms used in robotics [54].

Hypotheses: The requirements produced by this problem and in many other safety-critical problem domains (e.g., household caretaking, IMRT, assistive robots in epileptic patients, and disaster recovery) motivate the study of safety-aware motion planners with constraints. Therefore, **I hypothesize that a layered planning algorithm will find a hierarchical multi-planning sequences of motion that biases search into optimal mode transitions.** This layered composition of plans will first compute collision-free paths \mathcal{C}_{free} for moving the head between the start and goal poses. A higher hierarchical planning layer will then leverage encoded manipulation constraints within the robot-head interface to ensure that sensitive H&N structures are not damaged by radiation while the lower collision-free path in the hierarchy is to be executed. This layer of the planning algorithm might need to be repeatedly carried out in a fast computational loop to ensure all \mathcal{C} -space constraints are satisfied. Then a higher level plan takes the actions from the two previous lower level plans and generates a robustly stable controller in the sense of Lyapunov such that it can move the head along the \mathcal{C}_{free} paths even in the presence of parametric errors, or uncertainty in model dynamics [20, 55, 56]. **I further hypothesize that the overall hierarchical plan be sequentially structured so that head motion transitions between planning modes (i.e. from an initial location $\xi_i \in SE(3)$ to a goal region \mathcal{Q}_{goal}) are executed by leveraging online search protocols, which bias search for optimal and feasible paths to a sequence of modes that yield a smooth representation of head motion.** By these hypotheses, *I will address the current gap in geometric manipulation problems under manifold constraints that leave out stability analysis in the feedback control mode of the motion planner. I will achieve this by leveraging a Lyapunov-based stable estimator of the underlying dynamic system in safely generating optimally-robust single modes that guide transitions that precisely move the head.*

Procedure: I will formulate a stable geometrical representation of the underlying dynamical system and bias search toward optimally stable and robust short-task plans by providing an optimality-based method for choosing a control law once an robust control Lyapunov function (RCLF) [57] is known. I will develop an optimally stable and probabilistically-complete multi-modal planner that has broad applications to general multi-modal planning tasks in safety-critical problems in medical robotics.

A. Preliminaries: Let the set of all possible configurations of the head-robot system be \mathcal{Q} in the C-space \mathcal{C} [58]. Suppose that after a number synthesis of the proposed mechanism [59], the dimension of the robot is n . A particular configuration of the robot is defined by $\xi \in \mathcal{Q}$. We assume that the \mathcal{C} is a closed and bounded metric space, and that \mathcal{Q} is a measurable space $(\mathcal{Q}, \mathcal{B}_{\mathcal{Q}})$ for a $\mathcal{B}_{\mathcal{Q}}$ Borel σ -algebra on \mathcal{C} , generated from the metric [60]. The set of obstacles to be avoided are a closed set \mathcal{Q}_{obs} , which defines the free configuration space \mathcal{Q}_{free} , such that $\mathcal{Q}_{free} = cl(\mathcal{Q} \setminus \mathcal{Q}_{obs})^2$. Our goal is to find a path from ξ_i to some region of interest $\mathcal{Q}_{goal} \subset \mathcal{Q}$, i.e. a continuous injective map $\sigma : [0, 1] \rightarrow \mathcal{Q}_{free}$ such that $\sigma(0) = \xi_i$, and $\sigma(1) \in cl(\mathcal{Q}_{goal})$. In addition, a smooth positive definite and radially unbounded function $V(\xi)$ is a control Lyapunov function (CLF) for the head-robot control affine system $\dot{\xi} = f(\xi) + g(\xi, u)$ if

$$\frac{\partial V}{\partial \xi}(\xi)f(\xi) + \frac{\partial V}{\partial \xi}(\xi)g(\xi)q(\xi) \leq -P(\xi) \quad \forall \xi \neq 0 \quad (2)$$

where $P(\xi)$ is some positive definite function, $u \in \mathbb{R}^6$ is a control input, and $f(0, 0) = 0$.

B. An asymptotically stable in the large and optimal motion-planner: Our goal is to find an optimal collision-free path, c , with respect to a CLF $V(\xi) : \mathbb{R}^n \rightarrow \mathbb{R}^d$ such that

- $V(\xi)$ is positive for all $\xi \in \mathbb{R}^d \setminus \mathcal{Q}_{goal}$; and $V(\xi)$ exhibits a unique global minimum in the target region \mathcal{Q}_{goal} , where $V(\mathcal{Q}_{goal}) = 0$;
- as the head moves along any of the trajectories, we must have $V(\xi^{t,n}) > V(\xi^{t+1,n})$, and $V(\xi^{T^n,n}) = 0$; i.e. $V(\xi)$ decreases as time increases and $V(\cdot)$ vanishes when the actuators reach steady state after deformation;
- in addition, we require $V(\cdot)$ to satisfy the CLF requirement in (2)
- robust head motion during motion execution shall be guaranteed by devising *robust stabilizability via continuous state feedback* [57], provided that there exists an RCLF on the control-affine system.

We want to choose a control input $u = q(\xi)$ for some function $q(\xi)$ with $q(0) = 0$ so that equilibrium $\xi_e = 0$ of the closed-loop system

$$\dot{\xi} = f(\xi, q(\xi)) \quad (3)$$

is asymptotically stable in the large [61]. The first condition ensures the cost function is a valid Lyapunov function while the second option maintains the stability property in the sense of Lyapunov (i.e. \dot{V} being negative semi-definite for all $\xi \in \mathbb{R}^d \setminus \mathcal{Q}_{goal}$). To avoid wasting control energy and missing optimality during motion execution, as is common with the cancellation or domination of nonlinear terms in feedback linearization, the third option will leverage the *inverse optimal stabilization* in a differential game setting based on the pointwise min-norm control law of [57]. This is attractive because rather than solve a Hamilton-Jacobi-Isaacs (HJI) equation for a

² $cl(X)$ is the closure of a set, X .

control law that yields the path c , the pointwise min-norm control law yields a robustly stabilizable and optimal synthesis of the head motion correction problem.

C. Manifold Constraints: It is not enough for us to find a valid path c that is free of collisions. We also want the head motion to follow constraints that are functions of the robot's geometry, avoids radiation hitting critical structures, follows a path that does not increase proneness to claustrophobia [62], and lower the problem's dimensionality. Similar to [60], we define these *manifold constraints* to capture loop closure constraints, end-effector constraints etc. A forward kinematic map from the configuration of the i^{th} IAB, χ_{iab_i} , maps from respective IAB configurations to head position and orientation *i.e.* $K_{iab_i} : \chi_{iab_i} \rightarrow SE(3)$. The head velocity with respect to a fixed base frame in terms of IAB velocities can be written in terms of the forward kinematics Jacobian:

$$\begin{pmatrix} v_{iab_i} \\ \omega_{iab_i} \end{pmatrix} = \frac{\partial K_{iab_i}}{\partial \mathbf{r}_i} \frac{d\mathbf{r}}{dt} K_{iab_i}^{-1} = \mathbf{J}_i(\mathbf{r}_i) \dot{\mathbf{r}}_i \quad (4)$$

where \mathbf{r}_i is the spatial position of IAB i in generalized coordinates, and $(v_{iab_i}^T, \omega_{iab_i}^T) \in \mathbb{R}^6$ represents the linear and angular velocity of the i^{th} IAB about its screw basis. In essence, $\mathbf{r}_i \in \mathbb{R}^3$ with its rows are mapped to scalars by an appropriate choice of norm³. The contact between the head and the IABs is mapped by the Jacobian

$$\mathbf{J}_{c_i}(\xi_h, \xi_{iab_i}) = \begin{bmatrix} \mathbf{I} & \hat{\mathbf{w}}(r_{c_i}) \\ \mathbf{0} & \mathbf{I} \end{bmatrix} J_{r_i}, \quad (5)$$

where $\mathbf{J}_{c_i} : \dot{\xi}_{r_i} \rightarrow [v_{c_i}^T, w_{c_i}^T]^T$, $r_{c_i} \in \mathbb{R}^3$ is a vector between the head reference point (e.g. the center of mass) and the contact with the i^{th} IAB, ξ_h is the position and relative orientation of the head, ξ_{iab_i} is the position and relative orientation of the i^{th} soft robot in world coordinates, $\hat{\mathbf{w}}(r_{c_i})$ is an anti-symmetric matrix for the vector r_{c_i} , and $\xi_r = (\xi_{r_1}, \xi_{r_2}, \dots, \xi_{r_k})$, $(1 \leq k \leq n)$ are the positions and orientations for each of the IABs. For C^2 -smooth k -constraint functions G_1, \dots, G_k ($1 \leq k \leq n$), a constraint is fulfilled when $g_i(\xi) = 0$ and we write out the composite constraint function $G : \mathbb{R}^n \rightarrow \mathbb{R}^k$ with respect to the contact Jacobians as

$$G_i^T(\xi_h, \xi_{iab_i}) \xi_h = B_i^T(\xi_h, \xi_{iab_i}) \mathbf{J}_{c_i}(\xi_h, \mathbf{r}_i) \dot{\xi}_{iab_i} \quad (6)$$

for an IAB's selection matrix $B_i^T(\xi_h, \xi_{iab_i}) \in \mathbb{R}^{m_i}$, where m_i is the range of all the forces and moments for the chosen contact primitive (or union of contact primitives). Therefore, for k actuators in the soft robot, we have the following manipulation constraint

$$\begin{bmatrix} G_1^T \\ \vdots \\ G_k^T \end{bmatrix} \begin{pmatrix} v_h \\ w_h \end{pmatrix} = \text{diag} \begin{pmatrix} B_1^T \mathbf{J}_{c_1} \\ \vdots \\ B_k^T \mathbf{J}_{c_k} \end{pmatrix} \begin{pmatrix} \dot{\mathbf{r}}_{iab_1} \\ \vdots \\ \dot{\mathbf{r}}_{iab_k} \end{pmatrix}. \quad (7)$$

The details of this derivation are presented in my unpublished work [28]. We call \mathcal{M}_{free} the free constraint manifold of the overall manifold, \mathcal{M} , which is defined as $\mathcal{M}_{free} = \mathcal{M} \cap \mathcal{Q}_{free}$.

Problem 1 (Constrained RCLF Motion Planning). *Find an RCLF collision-free path $\sigma^* : [0, 1] \rightarrow \mathcal{M}_{free}$ given a path planning problem $(\mathcal{Q}_{free}, \xi_i, \mathcal{Q}_{goal})$, manipulation constraint, G , and cost function V such that $V(\sigma^*) = \min_{\sigma \in \Sigma_{\mathcal{M}_{free}}} V(\sigma)$ if one exists.*

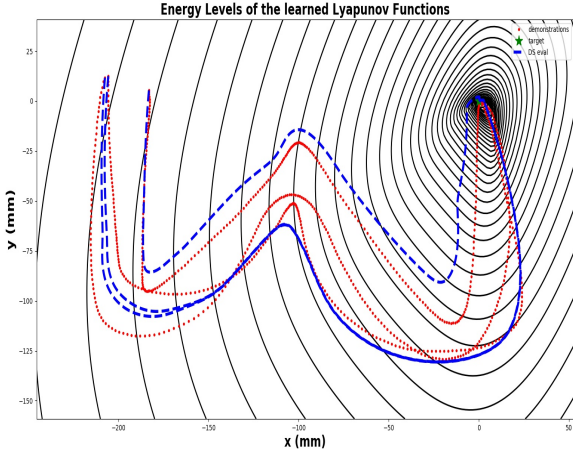
Expected results: Previously, the stabilizing command for items 1 and 2 in subsection B above was computed by solving a constrained optimization problem to choose the collision-free stabilizing command among the possible solutions. My implementation takes a greedy approach using the L-BFGS optimization algorithm with box constraints, in contrast to the quadratic nonlinear constrained optimization used by [63], to find the minimal value of the control law u at each time step such that u it is stable. Results of this implementation on toy robot nonlinear control from example demonstrations in 2D task space, implemented in python (see [64]), are reprinted in Fig. 10. When the problem identified in Prob. 1 is solved, I should expect my results to provide better trajectory tracking than the non-RCLF implementation I implemented in [64] owing to the account for all possible manifold constraints in the problem formulation.

K₉₉ Aim III: Mechanism Assembly. Phantom and Healthy Volunteer Experiments.

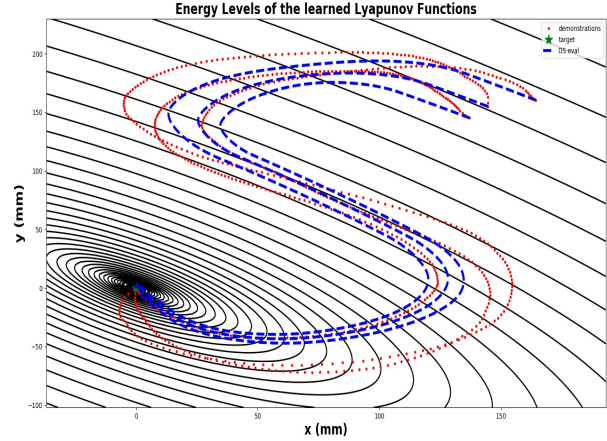
Rationale.

Case for a parallel soft manipulator: Open-loop kinematic chains have a low transportable load and poor accuracy since the weight of the segments that follow each link and the load of the structure contributes to the large flexure of torques; their links magnify errors from shoulder out to the end-effector, consequently hampering their use for sophisticated control strategies that may minimize or eliminate load-dependent error. Thus, most serially-joined manipulators are stiffened during the manufacturing process – thus, inherently exhibiting a high load-to-weight ratio and a complicated actuation system. Moreover, their passive bending stiffness overwhelms the degree of deformation. Parallel configurations, in spite of their higher number of actuated joints, distribute the weight of the load around the links of the robot, improve manipulation accuracy, have a desirable lightness property (albeit at the expense of a reduced workspace), and minimize the flexure torques that are otherwise common with open-loop kinematic chains. Given the non-cumulative nature of actuator errors in parallel configurations, greater precision is possible with minimal control-complication [65].

³I used the l_2 -norm in my implementation.

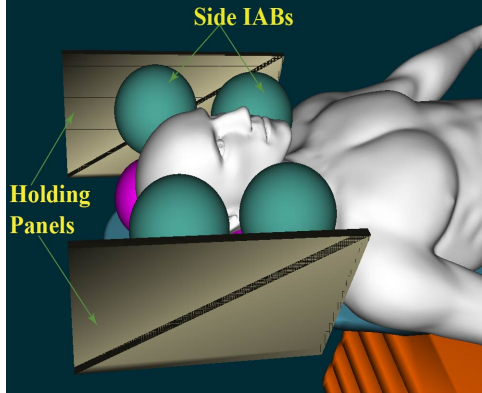


(a) Reproducing a nonlinear W-shape motion

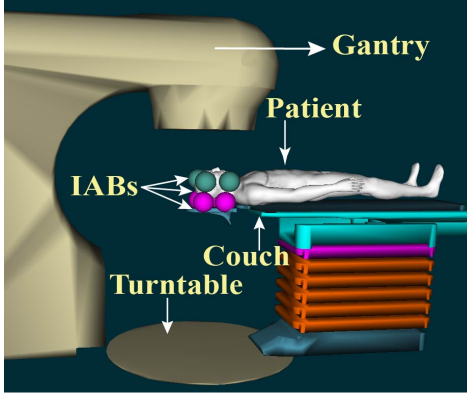


(b) Reproducing a nonlinear S-shape motion

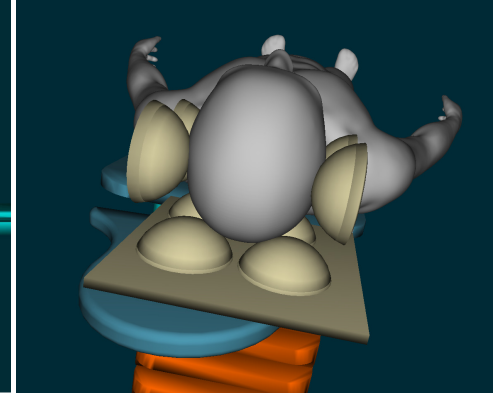
Figure 10: A CLF motion executor (red curves) that shows convergence to local attractors (green asterisks) and follows 3 different set trajectories (blue curves) for 2D nonlinear motion-trajectory problems on the WAM robot.



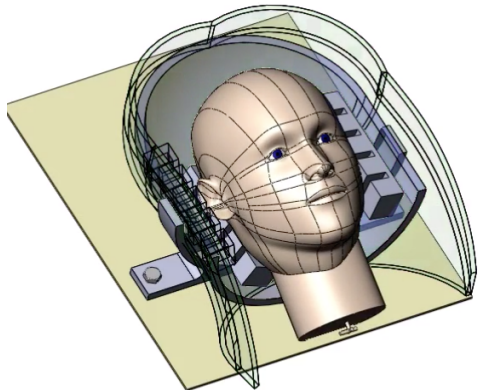
(a) Setup close-up view.



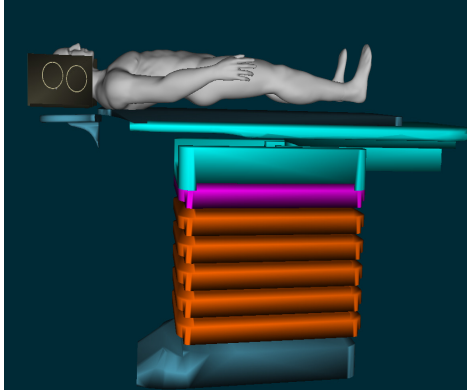
(b) Setup showing IMRT configurability.



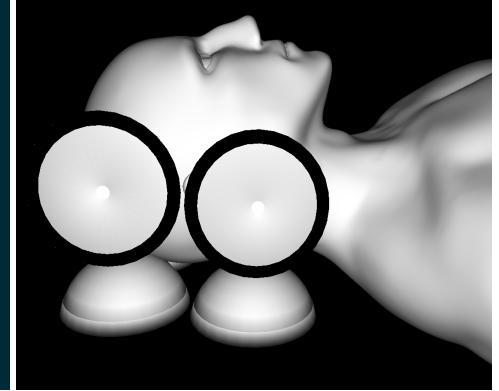
(c) SRS configurability setup with IAB Half-domes.



(d) Wearable setup under MRI Coils.



(e) Patient, IABs holders and couch.



(f) Patient-Robot System.

Figure 11: Proposed MRI-compatible LINAC patient motion compensation system.

Hypothesis.

Owing to the success of parallel robot mechanisms at precise manipulation tasks [2, 20, 66–68], **I hypothesize that a parallel soft-manipulator mechanism will yield the desired submillimeter and subdegree accuracy necessary for online, real-time head motion control in MRI-LINAC RT.**

Procedure.

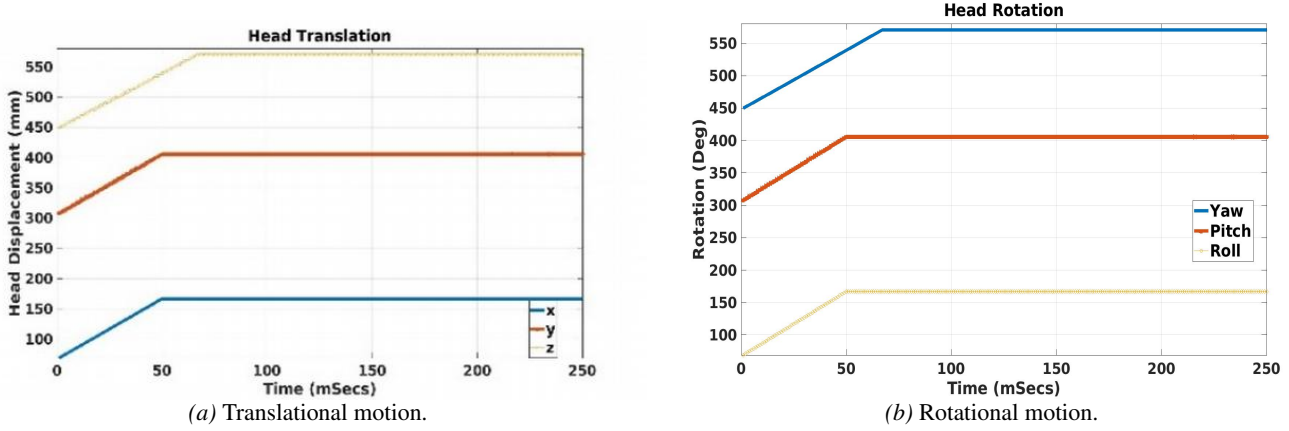


Figure 12: Open-loop setpoint-following for patient’s head motion in $\mathbb{SE}(3)$. Reprinted from [13].

A. Head Motion Correction in $\mathbb{SE}(3)$: I will systematically synthesize and analyze parallel soft robot manipulators for head and neck motion correction in MRI-LINAC systems. I will then leverage the kinematics and kinetics of soft manipulators which I proposed in [28] to construct the hierarchical motion planner in Aim II. Synthesizing multi-DOF parallel soft robots is challenging given the interdependency of the parameters that characterize the deformation, the individual robot constraints’ relative three dimensional orientation, permitted motion orientations, the three dimensional relation between constraints and allowed motions, and the possibility of multiple assembly modes that may result in the same end-effector pose [66]. The configuration that shall be investigated shall consist of soft actuators so arranged that their independent or coupled actuation can produce the needed head motion correction along the left-right (LR), the anterior-posterior (AP) , and/or the ssuperior-inferior (SI) axes. I will analyze the manipulation map, kinematics and kinetics of the respective closed-loop chains, and analyze the contact equations between the IAB system and head.

Fig. 11b shows an example standalone motion correction prototype for an IMRT system while Fig. 11c shows the proposed mechanism for MRI-LINAC systems (without MRI coils). Owing to the modular design, the coils of an MRI can be easily integrated onto this mechanism. In a parallel kinematic manner, the soft domes are positioned around the patient’s cranial region while the patient lies supine on a typical MRI/RT treatment couch (Fig. 11b). The soft domes will be held in place around the head by impact-resistant low-temperature rigid PVC foam insulation sheet that is encased in carbon fiber. Velcro stickers (not shown) will be affixed to the planar soft dome holders to accommodate different patient cranial geometry – thus providing a modularization that ensures re-usability for different patients. The side actuators will correct head motion along the LR axis of the head anatomy *i.e.* (yaw and roll motions), while the bottom ones will correct head motion along the AP direction. The SI motion will be adjusted by the two lower actuators on the bottom of the neck. These will conform deformation in a non-Gaussian fashion through an appropriate configuration of fiber-reinforcing (see [videos](#)). The domes underneath the forehead would control pure z translation and pitch rotatory motions.

In preliminary work [28], I have synthesized differential kinematics [69], continuum mechanics [70,71] and multi-bodied kinematics. Equation (7) yields the cranial manipulation constraint between the soft actuators and the head so that we can find the respective translational and rotational head velocity components, v_h, ω_h respectively in world frames. We can easily find the pseudo inverse of the manipulation map, G in (7), so as to determine head velocity on the treatment couch. The derivation of this equation is detailed in [27].

B. Expected Results: I would expect that my results will follow the open-loop head motion control simulation results in the SOFA [72] framework as presented in my recently accepted publication [13] using the proposed setup of Fig. 11f: raising or rotating the head in $\mathbb{SE}(3)$ resulted in steady-state reference trajectory tracking along all 6-DoFs of head motion as shown in Fig. 12.

R_{00} Aim: Patient oncological clinical trials.

To verify accuracy of delivered dose, a complete end-to-end evaluation of the robotic MRI-compatible RT system will be conducted using anthropomorphic phantom studies. From the preliminary data (Fig. 3, 5, 12), whereupon excellent agreement was found between head motion and given target trajectory using the adaptive controller proposed in [20]. Once we ascertain the efficacy of this, we will move to healthy human volunteer trials.

Statistical Plan: Phantom-based and healthy human volunteer trials will be conducted after we finish the design and build of the proposed system. A complete end-to-end testing with 3D printed head phantoms containing dosimetric gel will be used to evaluate 3D radiation dose accuracy for both single and multiple target MRI-compatible RT plans. A 20 volunteer study with a mock radiation beam will be conducted in a clinical environment to verify 6DOF head control and patient safety systems. A clinical study on 20 whole brain patients will be performed where validation of method will be determined by a statistical endpoint defining success as to whether or not the 6D intracranial target is $\leq 0.5\text{mm}$ and $\leq 0.5^\circ$ for greater than 95% of the treatment time.